13A.5 MICROPHYSICAL INTERPRETATION OF BOTH FAST ALTERNATING AND SIMULTANEOUS HORIZONTAL AND VERTICAL TRANSMIT DATA

J.C. Hubbert,* S. M. Ellis and W. Y. Chang

National Center for Atmospheric Research, Boulder, CO

1. Introduction

The polarimetric signatures from both simultaneous transmission of horizontal (H) and vertical (V) polarizations (SHV) and fast alternating H and V transmission (FHV) are modeled, analyzed and microphysically interpreted. The data show anomalies that are likely due to cross-coupling of the H and V transmitted waves due to aligned canted ice crystals. The experimental data comes from National Center for Atmospheric Research S-band radar, S-Pol, during TiMREX (Terrain-influenced Monsoon Rainfall Experiment). The S-Pol SHV data set is complemented by FHV data. The data are augmented with dual-Doppler and sounding data. T-matrix scattering simulations and a radar scatter model are used to explain the observed polarimetric signatures. A radar scattering model as well as T-matrix scattering simulations are used to explain the observed polarimetric signatures.

Many weather radars now achieve dual-polarization by transmitting simultaneously both horizontal (H) and vertical (V) polarized waves simultaneously (called SHV mode here but also referred to as STAR mode). It is well known that cross-coupling of these two components occurs when the transmitted wave propagates through ice crystals that are aligned and have some mean canting angle significantly away from horizontal (Ryzhkov and Zrnić 2007; Wang and Chandrasekar 2006; Hubbert et al. 2010a,b). Electric fields are known to align ice crystals (Hendry et al. 1982; Caylor and Chandrasekar 1996; Metcalf, J.I. 1995; Krehbiel et al. 1996) and cause negative K_{dp} (specific differential phase). Such aligned canted ice particles can bias not only Z_{dr}^{shv}, but also LDR (linear depolarization ratio) in fast alternating transmission of H and V polarizations operations (FHV mode). Biases in both Z_{dr}^{shv} and LDR are readily evident as radial stripes in range. S-Pol SHV and FHV data gathered during TiMREX in close time proximity are analyzed and used to infer the nature of the ice crystals that are responsible for the cross-coupling and resulting observed polarimetric signatures. Negative K_{dp} in the ice phase in smaller convective cells, which is fairly common in the TiMREX S-Pol data, are presented and discussed. High magnitudes of K_{dp} (both positive and negative) in the ice phase coupled with near zero values of Z_{dr}^{fhv} (FHV Z_{dr}) are explained and modeled as a population of two types of ice particles in the radar resolution volume: 1) aligned ice crystals that yield a high $|K_{dp}|$ and 2) randomly oriented larger ice aggregates or graupel that mask the high intrinsic Z_{dr} of the aligned ice crystals. This was also modeled by Kennedy and Rutledge (2011) who used the T-matrix method to simulate the backscatter cross-sections of populations of ice particles in winter storms. Here, the T-matrix method is also used but then the radar scattering model of Hubbert and Bringi (2003) is used to predict the bias in Z_{dr}^{shv} and LDR caused by cross-coupling. Dual-Doppler synthesis data along with sounding data are presented which support the microphysical interpretations.

*NCAR/EOL, Boulder, Colorado 80307, email: hubbert@ucar.edu

2. The TiMREX Data Set and Storm Overview

On 2 June 2008 both SHV and FHV data sets were gathered in close time proximity during TiMREX (Terrain-influenced Monsoon Rainfall Experiment). On this day, a north-south line of convective cells formed to the south of S-Pol with trailing stratiform rain to the west. The storm cells were moving west to east. This data set was also discussed in Hubbert et al. (2010b). In the following expanded analysis, K_{dp}, LDR, dual-Doppler synthesis and sounding data are added.

2.1. *Wind Vector Analysis, Sounding and Lightning Data*

The three-dimensional wind fields were retrieved via the variational multiple-Doppler radar wind synthesis method from Liou and Chang (2009). The conventional dual-Doppler synthesis method derives the vertical motion via upward/downward integration of the continuity equation with specified bottom/top boundary conditions. In contrast, the variational method derives the vertical motion via dynamical constraints and numerical smoothing terms including the anelastic continuity equation, the vertical vorticity equation, background wind, and spatial smoothness terms. The advantage of including the vertical vorticity equation is that there is no need to artificially prescribe the top or bottom boundary conditions for the vertical velocities in the traditional sense. Mewes and Shapiro (2002) have shown that the vertical vorticity equation helps determine the appropriate boundary conditions, which improves the recovery of the vertical velocities.

Four volume scans from two radars gathered on 2 June 2008 are used to construct the three-dimensional wind fields. Two volume scans from S-Pol were collected at 06:16:19 UTC and 06:24:30 UTC and the other two volumes were collected by the operational Doppler radar RCKT (Ken-Ting radar), operated by Central Weather Bureau (CWB) of Taiwan, at 06:16:56 UTC and 06:24:26 UTC. The radar data were processed to remove non-meteorological echo, to de-alias the folded radial velocities, and then interpolated to Cartesian coordinates. The low/upper level displacement due to system advection (the system motion was about 7.7 and 9.4 $\mathrm{m\,s^{-1}}$ in the x- and y-directions) were corrected as well. The synthesis domain was determined by considering the location of convective cells and the data coverage due to scanning strategy and topography of southern Taiwan. The horizontal and vertical resolutions of the retrieved wind fields are 1.0 and 0.5 km, respectively, and the upper boundary is 15.0 km to cover the echo top.

Figures 1 and 2 show storm-relative retrieved wind vectors from dual-Doppler wind analysis. Figure 1a-c show wind vectors overlaid on S-Pol reflectivity at 2.5 km, 5 km and 7.5km AGL, respectively. Figure 2a,b shows wind vectors overlaid on S-Pol reflectivity along, east-west cuts at 49 km and 59 km south of S-Pol through two small convective cells of interest. The convective cells show moderate updrafts of $2\,\mathrm{m\,s^{-1}}$ to $6\,\mathrm{m\,s^{-1}}$ between 5 km and 20 km in Fig. 2. Overlaid on the reflectivity plots of Fig. 1 are data from the lightning detection network of Taiwan. The red "X" indicate recorded in-cloud lightning discharges; there were no cloud-to-ground strikes recorded. Thus, there was electrification taking place in the general storm complex even though no flashes were recored in the convective cells of interest; however, the clouds still can be electrified. Peak reflectivity values of about 36 dBZ were observed at the $-10°$C level of these cells. The existence of 40 dBZ at the -10°C is a usual rule of thumb for the onset of lightning (Zipser and Lutz 1994).

Figure 3 shows a skew-T plot from a sounding taken at 06:00 UTC on 2 June at about 80 km southwest along the 148 radial of S-Pol, i.e., very close to the S-Pol radar data of Figs. 1, 2. The black and blue solid lines indicate the temperature and dewpoint temperature (deg C), respectively and the red dashed line is the estimated temperature (deg C) of a convective parcel. The sounding is typical of tropical environments with a temperature lapse rate that is nearly moist adiabatic and deep moisture that extends to about 9 km altitude. The estimated convective available potential energy (CAPE) is over 1400 J spread from sea level to about 14 km altitude. The estimated parcel temperature is never more than 3° or 4°C warmer than the environment. Thus this sounding supports deep convection with moderate updrafts and is consistent with the dual-Doppler observations of the presence of convective cells that reach up to almost 14 km and have maximum updraft speeds less than $10\,\mathrm{m\,s^{-1}}$. The sounding shows temperatures of -6.7°C at 6.2 km AGL, -20°C at 8 km AGL and $-38°$C at 10 km AGL with many levels at or near saturation.

From Figs. 1-3 we conclude that the air is very likely saturated or supersaturated within the significant updrafts and that the environment is conducive to ice crystal growth by both deposition and riming. If both crystals and graupel are present, it is likely that charge separation is occurring also (Zipser and Lutz 1994), leading to the presence of electric fields. The polarimetric signatures of this region and associated simulations shown below are consistent with the electrification hypothesis.

3. S-Pol Polarimetric Signatures from TiMREX

In this section the SHV and FHV polarimetric signatures gathered during TiMREX on 2 June 2008 corresponding to Figs. 1 and 2, are compared and analyzed, and a microphysical interpretation is given. Both data sets demonstrate the effects of cross-coupling during propagation due to aligned, canted ice particles. Figure 4 shows FHV Z, Z_{dr}, and ϕ_{dp} in the left hand column while SHV Z, Z_{dr}, and ϕ_{dp} are given in the right column. The FHV data were gathered at 6:19:36 UTC while the SHV data were gathered at 6:13:59 UTC, both at 8.6° elevation angle. Figure 5 shows the accompanying K_{dp}^{fhv}, K_{dp}^{shv}, LDR_h (Linear Depolarization Ratio for H transmit, hereafter referred to as just LDR) and ρ_{hv}^{fhv}. LDR, Z_{dr}^{fhv}, ρ_{hv}^{fhv} clearly show the melting level at the 30 km range ring. The ρ_{hv}^{shv} is not shown since it is very similar to ρ_{hv}^{fhv}.

Bias due to cross-coupling is evidenced by the radial stripes beyond the melting level in Z_{dr}^{shv} of Fig. 4e and in LDR of Fig. 5b (Ryzhkov and Zrnić 2007; Hubbert et al. 2010b). These radial stripes are caused by aligned ice particles that have a non-zero mean canting angle. The most prominent stripes in Z_{dr}^{shv} and LDR are delineated by three dashed lines: lines (x), (y) and (z) mark the FHV data plots while lines (u), (v) and (w) mark the SHV data plots. The middle lines mark approximately the radial where Z_{dr}^{shv} (LDR) decrease (increase) maximally. These two striped regions are the focus of our analysis and this S-Pol data set shows similar features as was discussed in Part 1.

Dashed line (w) for Z_{dr}^{shv} data of Fig. 4e marks the approximate right edge of the *decreasing*, likely biased Z_{dr}^{shv} area. This decreasing Z_{dr}^{shv} region begins at about 45 km and extends to roughly 65 km in range which corresponds to heights of 6.85 km and 9.97 km AGL, respectively. The two convective cells are seen in Fig. 4d marked by the higher reflectivities of about 35 dBZ along dashed line (w) at 50 km and 60 km range. These two cells are also seen in the two vertical wind vector cuts of Fig. 2. Beyond 65 km Z_{dr}^{shv} remains relatively constant along the radials between lines (u) and (w). The K_{dp}^{shv} of Fig. 5 show two small areas with negative values (maximum of $0.8°$ km^{-1}) with the larger area located along dashed line (w) also at roughly 60 km range. The two negative K_{dp}^{shv} areas roughly correspond to the two higher reflectivity areas. We infer that a local electric field was produced by the convection in these areas which vertically aligned the smaller ice particles, thus causing the negative K_{dp}^{shv}. We also infer that since decreasing Z_{dr}^{shv} mostly occurs between 45 km and 65 km, this is the region, between lines (w) and (u), where there are evidently aligned canted ice crystal causing the negative bias in Z_{dr}^{shv}.

Next examine LDR in Fig. 5b. Dashed lines (x), (y) and (z) mark the region where LDR increases from -27 dB to about -12 dB. The region is analogous to the above decreasing Z_{dr}^{shv} region: both are caused by cross-coupling due to aligned canted ice crystals. The region of the majority of the LDR increase is again roughly 45 km to 65 km. Thus, this area from 45 km to 65 km between lines (x) and (y) is analogous to the region in the SHV data from 40 km to 65 km between lines (u) and (w). The Z^{fhv} of Fig. 4a shows the two convective cores along the line (z) again at about 50 km and 60 km with peak reflectivities of about 33 dBZ. The two cores have advected to the east about 6 km during the 5.5 minute time difference between the FHV and SHV scans. The Z_{dr}^{fhv} can be considered as a much more accurate measurement in this region than Z_{dr}^{shv} since the effects of cross-coupling are negligible on Z_{dr}^{fhv} (Wang and Chandrasekar 2006). In the region of increasing LDR between lines (y) and (z), Z_{dr}^{fhv} is slightly positive on average. To the west between lines (x) and (y), Z_{dr}^{fhv} is a bit more positive, especially along line (x) where Z_{dr}^{fhv} is around 0.4 dB. In the next 15 km farther west beyond line (x), Z_{dr}^{fhv} is between 0.4 dB and 1 dB, most everywhere.

3.1. *Negative* $\mathbf{K_{dp}}$

Corresponding to the higher reflectivities along lines (z) and (w) are areas of negative K_{dp} marked in green color scale in both the SHV and the FHV data of Fig. 5a,c. The peak negative K_{dp} is approximately $-0.8°\text{km}^{-1}$ for both the SHV and FHV data. This is a relatively large value in the ice phase and indicates that there is a significant population of ice particles with their major axis oriented near vertical and with large major to minor axis ratios. Examining the Z_{dr}^{fhv}, it is seen that the intrinsic Z_{dr} in these regions is close to 0 dB. Simulations discussed below show that ice crystals that produce a K_{dp} of $-0.8°\text{km}^{-1}$ would also produce significantly negative Z_{dr}, smaller than -3 dB. Thus, in these regions there are likely two ice crystal population types 1) a high concentration of near vertically aligned small ice crystals with a high axis ratio, resulting in negative K_{dp}, and 2) larger ice particles that are randomly oriented and dominate the backscatter signature, thus producing a near zero Z_{dr}. Kennedy and Rutledge (2011) have also modeled oriented dendrites in winter storms over the Front Range of Colorado with larger aggregates that masked the higher Z_{dr} of the dendrites. Recently, Andrić et al. (2013) also compiled scattering calculations for vertical profiles of polarimetric radar data using different types of ice particles for a winter storm in Oklahoma. Their model, however, was unable to predict their higher observed K_{dp}. The radar data and dual-Doppler analysis above indicates that weak convection was taking place (vertical velocities of 2 to 6 m s^{-1}) so that that ice crystals (columns and plates) were being produced (Bailey and Hallett 2009). It is very likely that electrification was occurring which aligned the ice crystals.

Moving west of lines (z) and (w), the amount of cross-coupling increases, as is evidenced in the Z_{dr}^{shv} and LDR plots (Figs. 4e and 5b), until lines (y) and (v) which mark the radials of near maximum cross-coupling. Lines (y) and (v) also approximately mark the transition area between the negative K_{dp} and positive K_{dp} areas. Moving further to the west to lines (x) and (u), the amount of cross-coupling decreases while K_{dp} increases. These lines also mark the radials of maximum ϕ_{dp} accumulation as seen Fig. 4c,f. Reflectivities also decrease to 15-20 dBZ. The K_{dp} is high with a maximum of $1°\text{km}^{-1}$; however, Z_{dr}^{fhv} is only slightly positive around 0.5 dB on average. Again, this indicates that there are two ice crystal population types: 1) smaller, near horizontally aligned ice crystals that give high K_{dp} and 2) larger randomly oriented particles that mask the high Z_{dr} of the horizontally aligned crystals.

Summarizing, the polarimetric signatures indicate that along lines (z) and (w) there are vertically aligned ice crystals mixed with larger aggregates or graupel. The vertical alignment is very likely due to the presence of electric fields. Moving to the west, the electric field gives ice particles a mean canting angle of around 45° (see Part 1) along lines (y) and (v) where cross coupling is maximized. Moving farther west where there is apparent weak electric fields so that alignment does not occur, the ice crystals are aligned primarily by aerodynamic forcing along lines (x) and (u) where K_{dp} becomes quite positive, maximum ϕ_{dp} accumulation occurs and the cross-coupling is greatly reduced. Moving even farther west additional radial streaks in Z_{dr}^{shv} and in LDR are seen indicating that the ice crystal obtain mean canting angles significantly away from $0°$ so that cross-coupling occurs. However, the mean canting angle does not exceed $\pm 45°$ since K_{dp} remains positive. The observed negative K_{dp} at the far southern edge of the storm are due to low SNR and are artifacts of the K_{dp} algorithm rather than microphysics. Z_{dr}^{fhv} remains around 0 dB or slightly positive through the western region where K_{dp} is quite positive (0.3 to $0.8° \mathrm{km}^{-1}$) again indicating the coexistence of two populations of ice particle types as discussed above.

To illustrate the vertical structure of the negative K_{dp} and the accompanying radar signatures, Fig. 6 shows a radial vertical cross section of FHV Z, Z_{dr}, K_{dp} and ρ_{hv}, as labeled, along line (z) of Fig. 5a. In the area of negative K_{dp}, Z_{dr}^{fhv} is -0.1 to -0.3 dB, Z^{fhv} is 25 to 35 dBZ, and ρ_{hv}^{fhv} is quite high indicating good data quality.

Negative K_{dp} such as seen in Fig. 5a,c are fairly common in TiMREX data. The negative K_{dp} regions are associated with shallow convective cores. The reflectivities are in the 23 dBZ to 35 dBZ range, Z_{dr} is close to zero, ρ_{hv} is high (> 0.98) and typically, radial LDR streaks are associated indicating canted ice particles are causing cross-coupling. Thus, electric fields are likely present in these regions.

4. T-matrix Modeling of Ice Crystals

In order to corroborate the inferences about the types of ice particles that cause the observed polarimetric signatures, we next simulate ice particle backscatter cross sections.

4.1. *Model Description*

The scattering model used is described in Waterman (1969) and Vivekanandan et al. (1993), which employs the T-matrix method to calculate the 2×2 scattering matrix, then integrates over the specified size and orientation distributions and creates the 4×4 Mueller matrix. The wavelength is 11 cm. The model was modified so that arbitrary mean canting angles for ensembles of particles could be included. This was accomplished by using the Fisher distribution (Fisher 1953; Mardia 1972) which is equivalent to a two dimensional Gaussian distribution that has been mapped to a sphere. For details of the Fisher distribution, see Mardia (1972); Hubbert and Bringi (1996).

The T-matrix simulations model ice crystals as prolate spheroids (e.g., columns) or as oblate spheroids (e.g., plates, dendrites). The axis ratio (AR) is defined as

$$AR = \frac{\text{c-axis length}}{\text{a-axis length}} \tag{1}$$

where the c-axis is perpendicular to the ice crystal basal face and the a-axis is perpendicular to the c-axis. Thus, columns have axis ratios greater than one while plates have axis ratios less than one.

There are no in-situ measurements of ice particles for this storm. Rather than using a theoretically constructed PSD (Particle Size Distribution), we use a measured PSD gathered on 10 June 2001 in Florida as part of the ABFM (Airborne Field Mill) project, at 22:18:50 UTC at -19.5C where the electric field was E_z(kV/m)= -36.14. The idea is to examine particle distributions that occur in similar environmental conditions as in Taiwan convective storms with electric fields present. Figure 7 shows a PSD and particle images collected by the HVPS (High Volume Precipitation Spectrometer) (wider right hand side image field) and the 2D-C (two dimensional cloud particle imaging probe) probe (narrower lefthand side image field). The blue and red lines are the PSD deduced from the 2D-C and HVPS probes, respectively. Together they yield a total PSD. It is well known that the 2D-C probes can overestimate the number of smaller particles due scattering. For the PSD used here, software-based shattering corrections from Field et al. (2006) were used to minimize the shattering artifacts based on particle interarrival times. Examining Fig. 4 there are two higher reflectivity areas that mark the top of small convective cores at roughly 50 and 60 km along the dashed line (z) for FHV data and along dashed line (w) for SHV data. The dual-Doppler analysis and sounding data discussed earlier indicated that convection was present and that the rising air parcels are very likely saturated or supersaturated. These conditions are favorable for both ice crystal growth by vapor deposition (Bailey and Hallett 2009) as well as larger particle growth by riming. Simulations below show that high density, high axis ratio ice crystals (columns, needles and plates) are likely present. Charge separation is likely occurring in the convective regions, creating electric fields that in turn align ice crystals.

4.2. *Ice Particle Scattering Calculations*

In this section we show scattering calculations for prolate and oblate spheroids for an experimentally gathered PSD (particle size distribution) for various particle densities. The idea is not to ascribe the observed polarimetric signatures to exact ice particle types. Rather we show a series of simulations that allow us to describe the bulk character of ice particles that would cause the polarimetric signatures.

From the K_{dp} and Z_{dr} observations discussed above, it is likely that there are both smaller aligned ice crystals as well as larger randomly oriented ice aggregates or graupel present. Thus, the PSD of Fig. 7 is partitioned into two regimes, 1) smaller aligned ice columns or plates that will yield significant K_{dp}, and 2) larger randomly oriented ice aggregates or graupel (with near zero dB Z_{dr}), which will mask the high Z_{dr} signatures of the aligned ice crystals. This dichotomy is not completely arbitrary. The calculations of Weinheimer and Few (1987) show that electric field strengths in excess of $100\,\mathrm{kV\,m^{-1}}$ are required to align ice crystals with major diameters greater than 1 mm whereas smaller ice crystals can be aligned by fields less than $100\,\mathrm{kV\,m^{-1}}$. Since there was no lightning detected in the storm cells of interest, we assume that smaller electric field strengths were present so that larger ice particles might not be aligned. There was, however, an electrical discharge recorded about 30 km north of the storm cell marked by "B" and "B' " in Fig. 1 as indicated by the red X. Scattering simulations for the smaller ice crystals are give in Table 1 for ice columns and in Table 2 for plates for various densities, axis ratios and maximum diameters. Both the columns and plates are given a Fisher orientation distribution with their longer axes horizontal (mean) in the plane of polarization and with a distribution of angles defined by $\kappa = 600$ which is equivalent to a standard deviation of 3.5° (Hubbert and Bringi 1996). The maximum diameter is either 0.587 mm or 0.95 mm. The axis ratios used are in agreement with experimental observation (Ono 1969). Since the ice crystals are relatively small, the density is first taken as $0.917\,\mathrm{g\,cm^{-3}}$, i.e., solid ice. This density then yields an upper bound for K_{dp} and Z_{dr} for the assumed PSD. Rasmussen et al. (1999) list densities for different types of plates and dendrites with almost all categories having densities greater that $0.5\,\mathrm{g\,cm^{-3}}$ (an exception are stellar dendrites with a density of $0.44\,\mathrm{g\,cm^{-3}}$). Thus our simulations are repeated for a density of $0.5\,\mathrm{g\,cm^{-3}}$ and the results are given in Tables 1 and 2. From these tables several observations can be made about the bulk nature of the ice crystals. For a density of $0.5\,\mathrm{g\,cm^{-3}}$, the K_{dp} values are less than the experimentally observed $0.8^\circ\,\mathrm{km^{-1}}$. However, K_{dp} could be increased by increasing the number density of the ice particles; otherwise, it is likely that the ice particles have densities greater than $0.5\,\mathrm{g\,cm^{-3}}$. It can be inferred that for ice crystals less than 1 mm for the PSD considered here, the density needs to be greater than $0.5\,\mathrm{g\,cm^{-1}}$ to achieve the observed K_{dp} of $0.8^\circ\mathrm{km^{-1}}$. This would exclude stellar dendrites as a possible particle type. If the density is close to solid ice, only particles with diameters of ≤ 0.587 mm need to be aligned in order to yield K_{dp} of $0.8^\circ\,\mathrm{km^{-1}}$ or greater. Thus, weaker electric fields are sufficient to align these smaller ice particles.

The experimentally-observed negative K_{dp} indicates that there were aligned ice crystals with their longer axis near vertical. For plates with their major axis vertical, aerodynamic torque would not align the shorter axes (c-axis) so that they would be free to rotate around their longer aligned axes and this would reduce the magnitude of both K_{dp} and Z_{dr}. Foster and Hallett (2008) show that strong non-uniform electric fields can provide a secondary electric torque that could align the c-axis of the vertically oriented plates. However, it is not necessary that the c-axis be aligned in order to obtain negative K_{dp}. This is demonstrated next with simulations. The a-axis (longer axis) of the plates modeled in Table 2 are given a Gaussian distribution so that the mean canting angle is vertical with a standard deviation of 3.5°. The c-axis is given a uniform random orientation distribution. The results are given in Table 3 for a density of $0.917\,\mathrm{g\,cm^{-3}}$. The magnitude of K_{dp} has been reduced by about a factor of 2 as compared to Table 2. Thus, vertically aligned high density plates can produce the experimentally observed negative K_{dp}. Obviously, from Table 1, vertically aligned ice columns can give the required negative K_{dp} also.

5. Modeling Propagation Effects

The radar scattering model of Hubbert et al. (2010a) is now used which demonstrates the observed cross-coupling signatures in Z_{dr}^{shv} and LDR. Here we arbitrarily choose ice columns with a maximum size of 0.95 mm, an axis ratio of 3, and a density of $0.7\,\mathrm{g\,cm^{-3}}$. The T-matrix simulations are: $Z = 21.2$ dBZ, $Z_{dr} = 3.20$ dB, and $K_{dp} = 0.84^\circ\,\mathrm{km^{-1}}$, the latter matching well the experimentally observed K_{dp}. We note that even if the standard deviation of canting angles is increased from 3.5° to 15°, K_{dp} is only reduced to $0.76^\circ\,\mathrm{km^{-1}}$. $Z_{dr} = 3.20$ dB is much higher than the experimentally observed 0 to 1 dB Z_{dr}^{fhv} (Fig. 4b). The remaining larger particles (> 0.95 mm) from the PSD of Fig. 7 are now modeled as graupel with a 0.9 axis ratio and a uniform random orientation distribution. The bulk density is $0.3\,\mathrm{g\,cm^{-3}}$. The T-matrix simulation results for the graupel are $Z = 35.7$ dBZ, $Z_{dr} = 0$ dB, $K_{dp} = 0$. The ice columns are now given a mean canting angle that is vertical and then combined with the graupel. The simulation gives: $Z = 35.9$ dBZ, $Z_{dr} = -0.1$ dB, $K_{dp} = -0.84^\circ\,\mathrm{km^{-1}}$. If the density of the graupel is reduced to $0.2\,\mathrm{g\,cm^{-3}}$ then $Z = 32.5$ dBZ, $Z_{dr} = -0.17$ dB, $K_{dp} = -0.84^\circ\,\mathrm{km^{-1}}$. This simulation shows how it is possible to achieve relatively high reflectivities, negative K_{dp} and small negative Z_{dr}^{fhv} as is shown in Fig. 6.

Clearly there are many combinations of particle parameters (PSD, density, etc.) that will result in the simulated and observed polarimetric values. However, to obtain reflectivities greater than 30 dBZ, negative K_{dp} and near 0 dB Z_{dr} requires some combination of small vertically aligned crystals combined with larger, nearly spherical particles. It is interesting to note that it is possible to simulate columnar ice with observed PSDs that are small enough to be vertically aligned by relatively weak electric fields and result in the observed polarimetric signatures. This lends some confidence that the scenario described above is plausible in nature even though we do not have direct observations of it.

To model the bias caused by propagation effects, we now give the ice columns a mean canting angle of 45° and let the density of the graupel be $0.2\,\mathrm{g\,cm^{-3}}$. This density is perhaps low for graupel but this is done better match the observed reflectivity along lines (y) and (v) in Fig. 4. The PSD for the larger ice particles could also be changed by we choose to continue to use the PSD of Fig. 7 for continuity. This will minimize K_{dp} while maximizing the cross-coupling and the corresponding bias in SHV Z_{dr} and LDR. The modeled results are: $Z = 32.4\,\mathrm{dBZ}$, $Z_{dr} = 0\,\mathrm{dB}$, $K_{dp} = 0^\circ\,\mathrm{km}^{-1}$ and $LDR = -27.5\,\mathrm{dB}$. The covariance matrix for the ensemble (not given here) then

describes FHV data for the backscatter volume and does not account for propagation effects. To include propagation effects, and to simulate SHV data, the model presented in Hubbert et al. (2010a) is used. The propagation medium is given a mean canting angle of 45° and the covariance matrix generated from the model above for ice columns canted at 45° mixed with graupel is used to model the backscatter medium. Note that the larger randomly oriented ice particles do not affect the propagation matrix. Figure 8 shows Z_{dr}^{shv} (solid curve) and LDR_h (dashed curve) that result from the model, plotted as a function of principal plane ϕ_{dp}. As can be seen, after 25° of principal plane ϕ_{dp}, Z_{dr}^{shv} decreases to -2.5 dB and LDR increases to -13 dB which mimics the behavior seen along dashed lines (y) and (v) of Fig. 4d and Fig. 5b.

Z_{dr}^{shv} is a strong function of the transmit differential phase ($\arg\{E_v^t E_h^{t*}\}$) as was shown in Part 1 Fig. 4. For Fig. 8 the transmit differential phase was chosen as -40° since this value gave model results that match well the experimental data. The transmit differential phase of S-Pol is unknown.

The K_{dp} along dashed lines (x) and (u) between 45 km and 60 km range is positive with a maximum of $0.85^\circ\,\mathrm{km}^{-1}$. The reflectivies are 15 dBZ to 20 dBZ and Z_{dr}^{fhv} becomes more positive by a few tenths of a dB as compared to the negative K_{dp} regions along dashed line (z) and (w). Thus, the nature of the ice crystals has changed in this region; however, for continuity, the PSD of Fig. 7 is again used. In order to achieve these lower reflectivities with high K_{dp}, the aligned small crystals need a smaller Dmax. Thus, the Dmax is reduced to 0.437 mm. Again, since Z_{dr} is relatively small, these smaller ice crystals exist with larger randomly oriented ice particles. Accordingly, plates are modeled with a density of $0.87\,\mathrm{g\,cm^{-3}}$ with an axis ratio of 0.1. The results are: $Z = 10.6\,\mathrm{dBZ}$, $Z_{dr} = 7.57\,\mathrm{dB}$, $K_{dp} = 0.70^\circ\,\mathrm{km}^{-1}$. The larger ice particles greater than 0.437 mm are given a density of $0.05\,\mathrm{g\,cm^{-3}}$ (more indicative of aggregates). The results are $Z = 20.3\,\mathrm{dBZ}$, $Z_{dr} = 0\,\mathrm{dB}$, $K_{dp} = 0^\circ\,\mathrm{km}^{-1}$. Combining the aligned plates with the larger particles gives, $Z = 20.7\,\mathrm{dBZ}$, $Z_{dr} = 0.37\,\mathrm{dB}$, $K_{dp} = 0.71^\circ\,\mathrm{km}^{-1}$. This then matches fairly well the observed average radar signatures along dashed lines (x) and (u).

6. Summary and Conclusions

In this paper cross-coupling of simultaneously transmitted H and V waves, due to canted ice crystals, was observed, simulated and analyzed. Microphysical interpretation were offered. Both SHV and FHV S-Pol data from TiMREX were examined in detail. The analyzed SHV data and FHV data were gathered within 5.5 minutes of each other in a convective storm complex so that polarimetric signatures could be compared. Cross-coupling in the ice phase was evident from radial steaks in Z_{dr}^{shv} and LDR. Three regions surrounding the cross-coupling signatures were examined and micophysically interpreted: 1) an area with negative K_{dp}, Z_{dr} of about 0 dB and high reflectivity, 2) an area with small K_{dp}, near zero Z_{dr}, maximum cross-coupling and somewhat smaller reflectivity and 3) an area with high positive K_{dp}, small positive Z_{dr} (about 0.5 dB on average), maximum ϕ_{dp} accumulation and small cross-coupling. All three areas can be characterized by two distinct populations of ice particles, 1) smaller aligned ice crystals (columns or plates) with large major to minor axis ratios that cause large K_{dp} with relatively small reflectivity and 2) larger randomly oriented ice particles with larger reflectivity that mask the Z_{dr} of the smaller aligned ice crystals. Sounding data and dual-Doppler analysis showed that moderate updrafts, 2 to $6\,\mathrm{m\,s^{-1}}$ were present in a humid environment and likely resulted in supersaturated conditions, supercooled liquid water and rimed particles in the convective updrafts. Because of the observed negative K_{dp} (minima of $-0.8^\circ\,\mathrm{km}^{-1}$), an electric field was likely present that aligned the columns or plates of high axis ratio and high density. Since the reflectivity was high in this region and Z_{dr} was close to zero, larger graupel particles were likely present. The presence of ice crystals with graupel and supercooled liquid in an updraft are conditions conducive for charge separation. The negative K_{dp} was observed at other times and in other storms of similar composition and character: moderate storm depth with likely moderate updrafts, high reflectivities in ice, 6 to 10 km AGL, high ρ_{hv} and near zero Z_{dr}. Both LDR streaks and high K_{dp} areas are typically associated with the negative K_{dp} areas in many smaller convective cells observed by S-Pol during TiMREX. The ensuing electric field could further accelerate ice crystal growth and possible fragmentation so that there is an abundance of small crystals with high axis ratios that are able to cause the observed high K_{dp}.

Simultaneous transmission of H and V polarization waves is now a popular way to construct dual-polarization radar systems. Understanding of the polarimetric signatures presented in this paper is vital for correct microphysical interpretation of SHV data.

Acknowledgment The National Center for Atmospheric Research is sponsored by the National Science Foundation. Any opinions, findings and conclusions or recommendations expressed in this publication are those of the authors and do not necessarily reflect the views of the National Science Foundation. Several people were integral to the successful compilation of this paper. We would like to thank Drs. G. Wang and V.N. Bringi who supplied and assisted with the scattering code for the simulations. Drs. A. Bansemer and J. Dye supplied the PSD data and plot used in the paper. Dr. Steve Rutledge provided valuable discussion on the microphysics. Dr. Y.-C. Liou of the Department of Atmospheric Sciences, National Central University, Jhongli City, Taiwan created the dual-Doppler analysis code. Mr. Phillip Stauffer created the Skew-T plot.

References

Andrić, J., M. Kumajian, D. Zrnić, J. Straka, and V. Melnikov, 2013: Polarimetric signatures above the melting layer in winter storms: An observational and modeling study. *J. Appl. Meteor. Climat.*, **52**, 682–700.

Bailey, M. and J. Hallett, 2009: A comprehensive habit diagram for atmospheric ice crystals: Confirmation from the laboratory, AIRS II and other field studies. *J. Atmos. Sci.*, **66**, 2888–2899.

Caylor, I. and V. Chandrasekar, 1996: Time-varying ice crystal orientation in thunderstorms observed with multiparameter radar. *IEEE Trans. Geosci. Remote Sensing*, **34**, 847–858.

Field, P., A. Heymsfield, and A. Bansemer, 2006: Shattering and particle interarrival times measured by optical array probes in ice clouds. *J. Atmos. Oceanic Tech.*, **23**, 1357–1371.

Fisher, R., 1953: Dispersion on a sphere. *Proc. Roy. Soc. Lond.*, **A217**, 295–305.

Foster, T. and J. Hallett, 2008: Enhanced alignment of plate ice crystals in a non-uniform electric field. *Atmos. Res.*, **90**, 41–53.

Hendry, A., G. McCormick, and Y. Antar, 1982: Radar observations of polarization characteristics and lightning-induced realignment of atmospheric ice crystals. *Radio Science*, **17**, 1243–1250.

Hubbert, J. and V. Bringi, 1996: Specular null polarization theory: Applications to radar meteorology. *IEEE Trans. Geosci. Remote Sensing*, **34**, 859–873.

— 2003: Studies of the polarimetric covariance matrix: Part II: Modeling and polarization errors. *J. Atmos. Oceanic Technol.*, 1011–1022.

Hubbert, J., S. Ellis, M. Dixon, and G. Meymaris, 2010a: Modeling, error analysis and evaluation of dual polarization variables obtained from simultaneous horizontal and vertical polarization transmit radar. Part I: Modeling and antenna errors. *J. Atmos. Oceanic Technol.*, **27**, 1583–1598.

— 2010b: Modeling, error analysis and evaluation of dual polarization variables obtained from simultaneous horizontal and vertical polarization transmit radar. Part II: Experimental data. *J. Atmos. Oceanic Technol.*, **27**, 1599–1607.

Kennedy, P. C. and S. A. Rutledge, 2011: S-band dual-polarization radar observations of winter storms. *J. Appl. Meteor.*, **50**, 844–858.

Krehbiel, P., T. Chen, S. McCray, W. Wilson, G. Gray, and M. Brook, 1996: The use of dual channel circular polarized radar observations for remotely sensing storm electrification. *J. Meteor. Atmos. Phys.*, **59**, 65–82.

Liou, Y.-J. and Y.-J. Chang, 2009: A variational multipledoppler radar three-dimensional wind synthesis method and its impacts on thermodynamic retrieval. *Mon. Wea. Rev.*, **137**, 3992–4010.

Mardia, K., 1972: *Statistics of Directional Data*. Academic Press, New York and London.

Metcalf, J.I., 1995: Radar observations of changing orientations of hydrometeors in thunderstorms. *J. of Appl. Meteor.*, **34**, 757–772.

Mewes, J. and A. Shapiro, 2002: Use of the vorticity equation in dual-doppler analysis of the vertical velocity field. *J. Atmos. Oceanic Technol.*, **19**, 543–567.

Ono, A., 1969: The shape and riming properties of ice crystals in natural clouds. *J. Atmos. Sci.*, **26**, 138–147.

Rasmussen, R., J. Vivekanandan, J. Cole, B. Myers, and C. Masters, 1999: The estimation of snowfall rate using visibility. *J. Atmos. Sci.*, **38**, 1542–1563.

Ryzhkov, A. and D. Zrnić, 2007: Depolarization in ice crystals and its effect on radar polarimetric measurements. *J. Atmos. Oceanic Tech.*, **24**, 1256–1267.

Vivekanandan, J., R. Raghavan, and V. Bringi, 1993: Polarimetric radar modeling of mixtures of precipitation particles. *IEEE Trans. on Geoscience and Remote Sen.*, **31**, 1017–1030.

Wang, Y. and V. Chandrasekar, 2006: Polarization isolation requirements for linear dual-polarization weather radar in simultaneous transmission mode of operation. *IEEE Trans. Geosc. and Remote Sen.*, **44**, 2019–2028.

Waterman, P., 1969: Scattering by dielectric particles. *Alta Frequeza,(Speciale)*, 348–352.

Weinheimer, A. and A. Few, 1987: The electric field alignment of ice particles in thunderstorms. *J. Geophys. Res.*, **92**, 14833–14844.

Zipser, E. and K. Lutz, 1994: Vertical profile of radar reflectivity of convective cells: A strong indicator of storm intensity and lightning probability. *Mon. Wea. Rev.*, **122**, 1751–1759.

Table 1: *Modeled data for ice columns using the Fisher orientation distribution. The density is 0.917g cm*$^{-3}$*, (i.e., solid ice). Kappa*= 600.

density $\mathrm{g\,cm^{-3}}$	**axis ratio**	**Dmax (mm)**	Z (dBZ)	Z_{dr}(dB)	K_{dp} °km^{-1}
0.917	2	0.587	15.9	2.78	0.57
0.917	3	0.587	16.8	3.91	0.84
0.917	4	0.587	17.3	4.57	1.0
0.917	5	0.587	17.6	4.97	1.11
0.917	6	0.587	17.8	5.23	1.18
0.917	7	0.587	17.9	5.40	1.23
0.917	3	0.95	23.6	3.90	1.31
0.917	4	0.95	24.2	4.57	1.56
0.917	5	0.95	24.5	4.97	1.73
0.5	2	0.587	10.3	1.56	0.18
0.5	3	0.587	10.7	2.21	0.26
0.5	4	0.587	11.0	2.58	0.31
0.5	5	0.587	11.2	2.79	0.33
0.5	6	0.587	11.3	2.93	0.35
0.5	7	0.587	11.3	3.02	0.36
0.5	3	0.95	17.6	2.23	0.41
0.5	4	0.95	17.9	2.58	0.48
0.5	5	0.95	18.0	2.79	0.52

Table 2: *Modeled data for ice plates using the Fisher orientation distribution. The density is 0.917g cm*$^{-3}$*, (i.e., solid ice). Kappa*= 600.

density $\mathrm{g\,cm^{-3}}$	**axis ratio**	**Dmax (mm)**	Z (dBZ)	Z_{dr}(dB)	K_{dp}(°km^{-1})
0.917	0.1	0.587	17.4	7.88	1.49
0.917	0.2	0.587	16.6	6.28	1.17
0.917	0.3	0.587	15.9	4.98	0.92
0.917	0.4	0.587	15.4	3.90	0.72
0.917	0.1	0.95	24.3	7.88	2.32
0.917	0.2	0.95	23.4	6.28	1.81
0.917	0.3	0.95	22.8	4.98	1.43
0.5	0.1	0.587	11.0	4.66	0.50
0.5	0.2	0.587	10.6	3.72	0.40
0.5	0.3	0.587	10.3	2.96	0.32
0.5	0.4	0.587	10.0	2.32	0.25
0.5	0.1	0.95	17.9	4.66	0.77
0.5	0.2	0.95	17.5	3.72	0.62
0.5	0.3	0.95	17.2	2.96	0.49

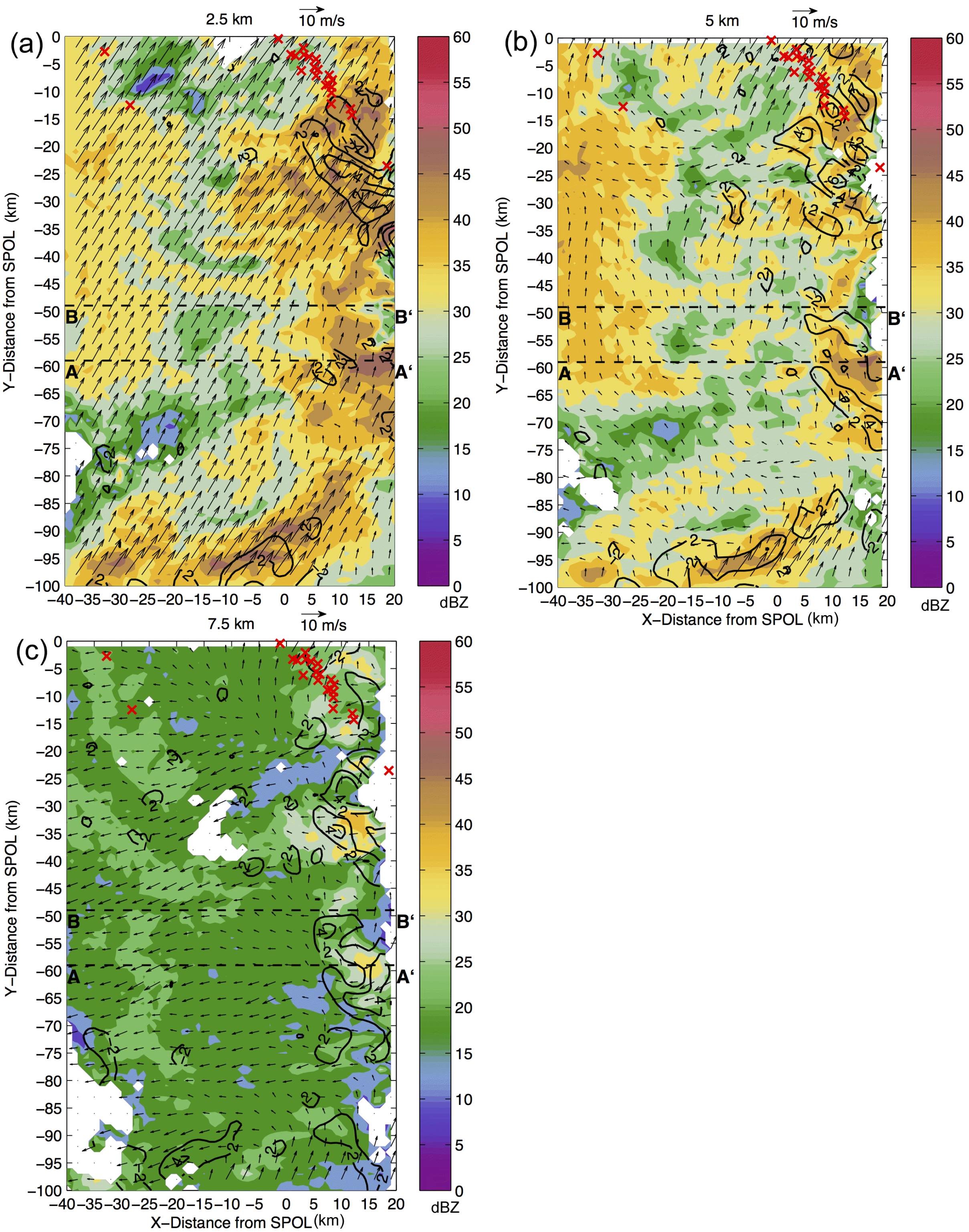

Figure 1: *Storm relative dual-Doppler wind vectors overlaid onto reflectivity at (a) 2.5 km AGL, (b) 5 km AGL and (c) 7.5 km AGL. Positive and negative vertical velocities ($m\,s^{-1}$) are in solid and dashed contours, respectively. Small red “X” denote where electrical discharges were recoded by the Taiwan lightning detection network.*

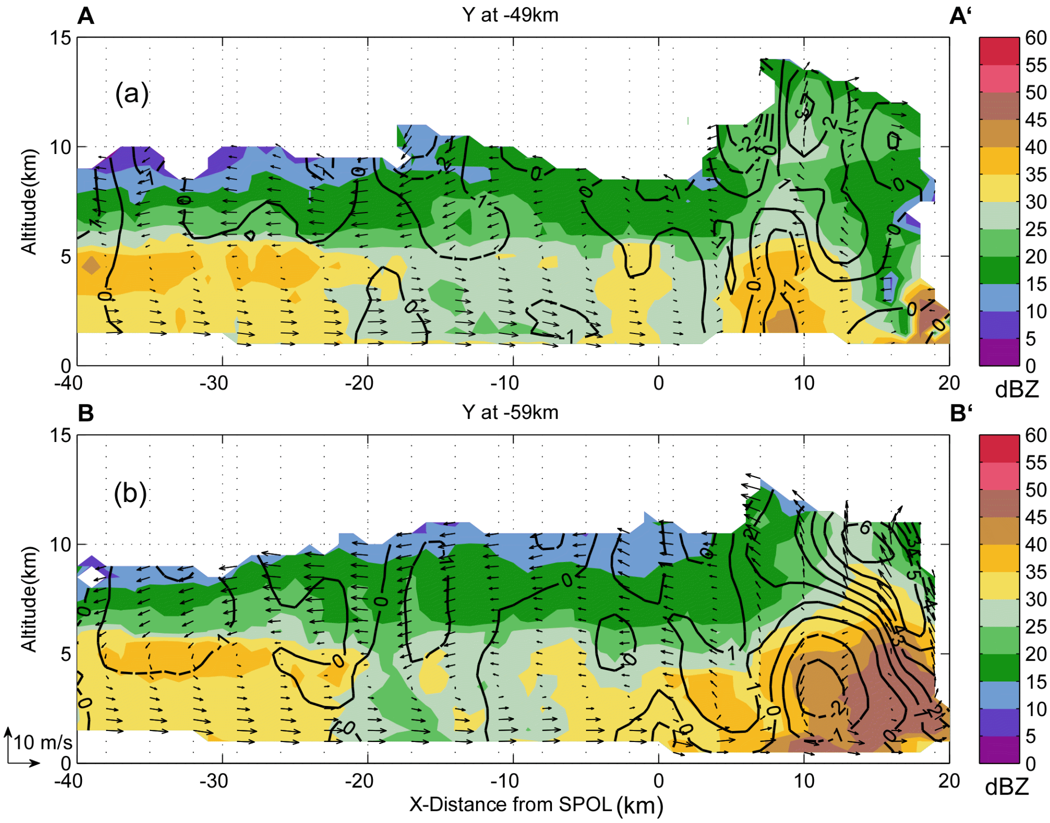

Figure 2: *Storm relative dual-Doppler wind vectors overlaid on east-west vertical cross-section of reflectivity (a) X=-49 km and (b) -59 km. Positive and negative vertical velocities ($m\,s^{-1}$) are in solid and dashed contours, respectively. Dashed lines on Fig. 1 show the location of the vertical cross-sections.*

Table 3: *Modeled data for vertically oriented ice plates. The density is 0.917g cm^{-3}, (i.e., solid ice). The plates' longer axes are oriented vertical with a standard deviation of $3.5°$. The c-axes are distributed uniform random in the horizontal plane.*

axis ratio	**Dmax (mm)**	Z (dBZ)	Z_{dr}(dB)	K_{dp}($^{\circ}$km^{-1})
0.1	0.587	14.7	-2.68	-0.74
0.2	0.587	14.2	-2.31	-0.58
0.3	0.587	14.0	-1.96	-0.46
0.1	0.95	21.6	-2.68	-1.15
0.2	0.95	21.1	-2.31	-0.90
0.3	0.95	20.8	-1.96	-0.71

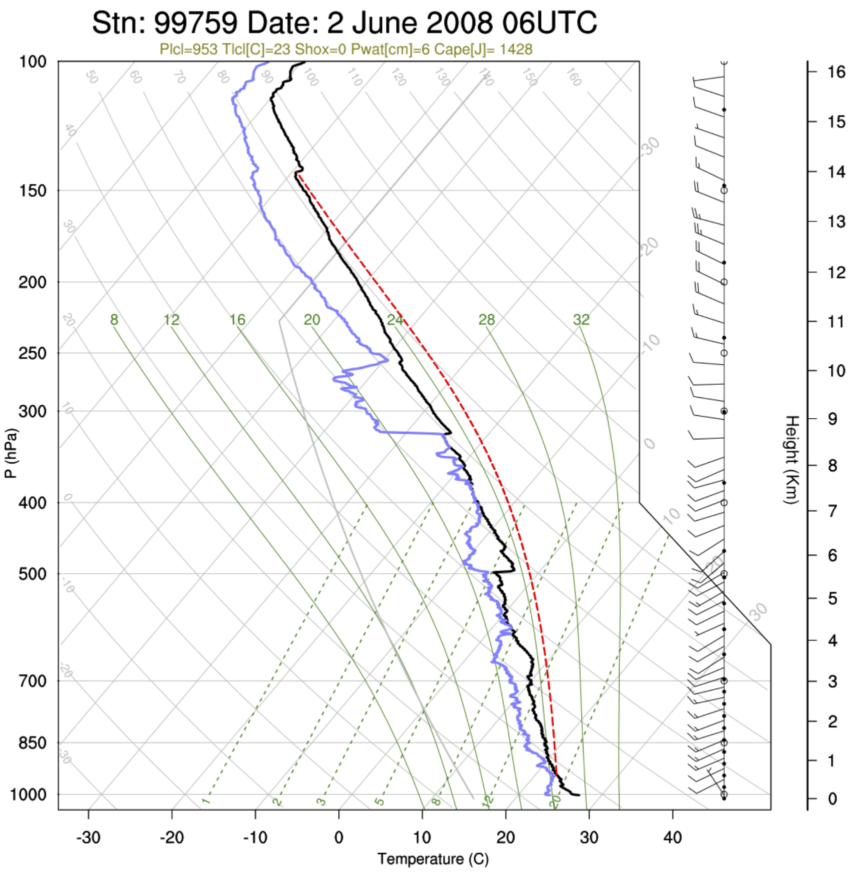

Figure 3: *A Skew-T plot from a TiMREX sounding gathered at 06:00UTC from the southern tip of Taiwan about 80 km away from the S-Pol site along the 148° radial. The black and blue solid lines indicate the temperature and dewpoint temperature (deg C), respectively and the red dashed line is the estimated temperature (deg. C) of a convective parcel.*

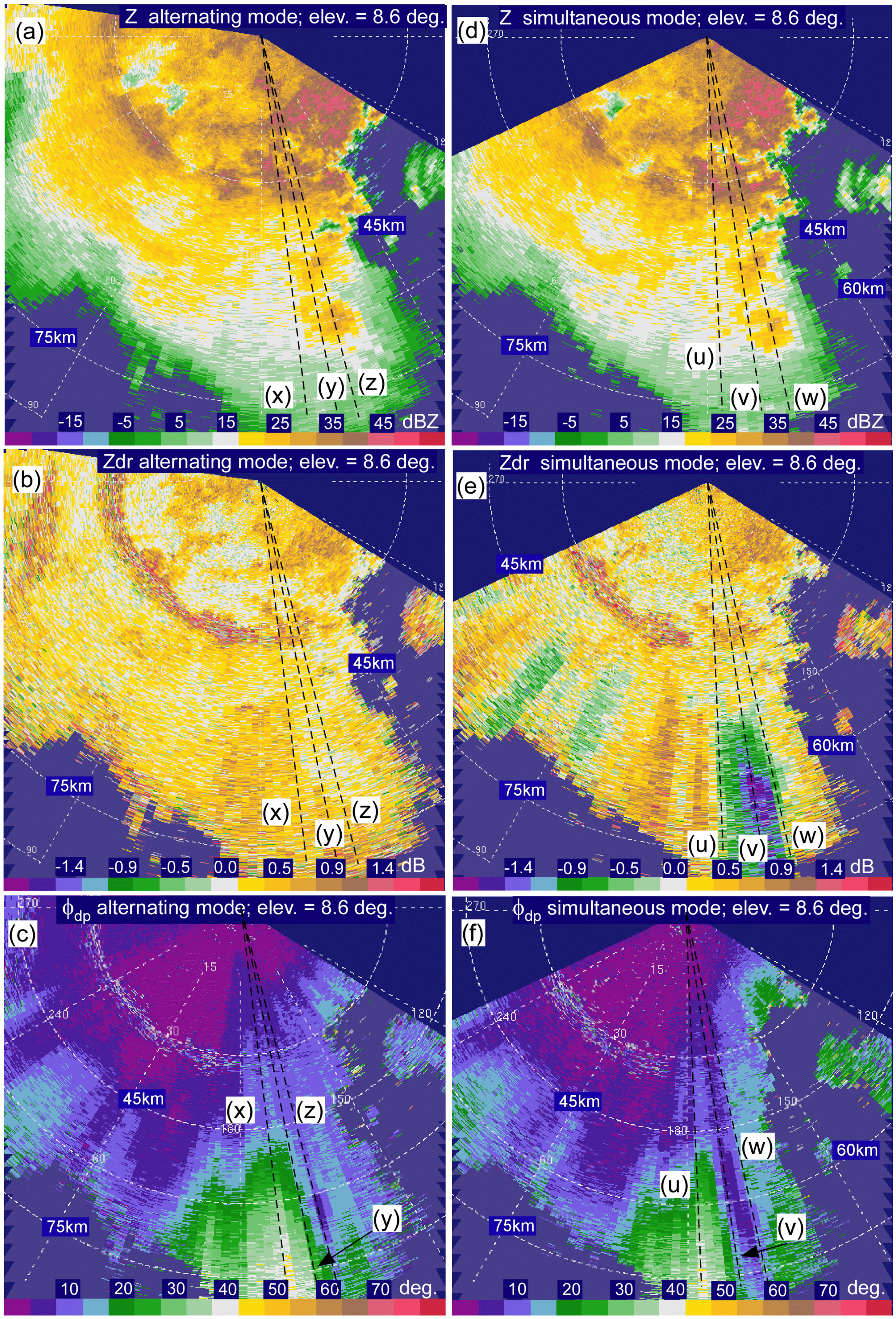

Figure 4: *S-Pol data from TiMREX. Lefthand side is FHV data while the righthand side is SHV data. The FHV and SHV data are separated by 5.5 minutes.*

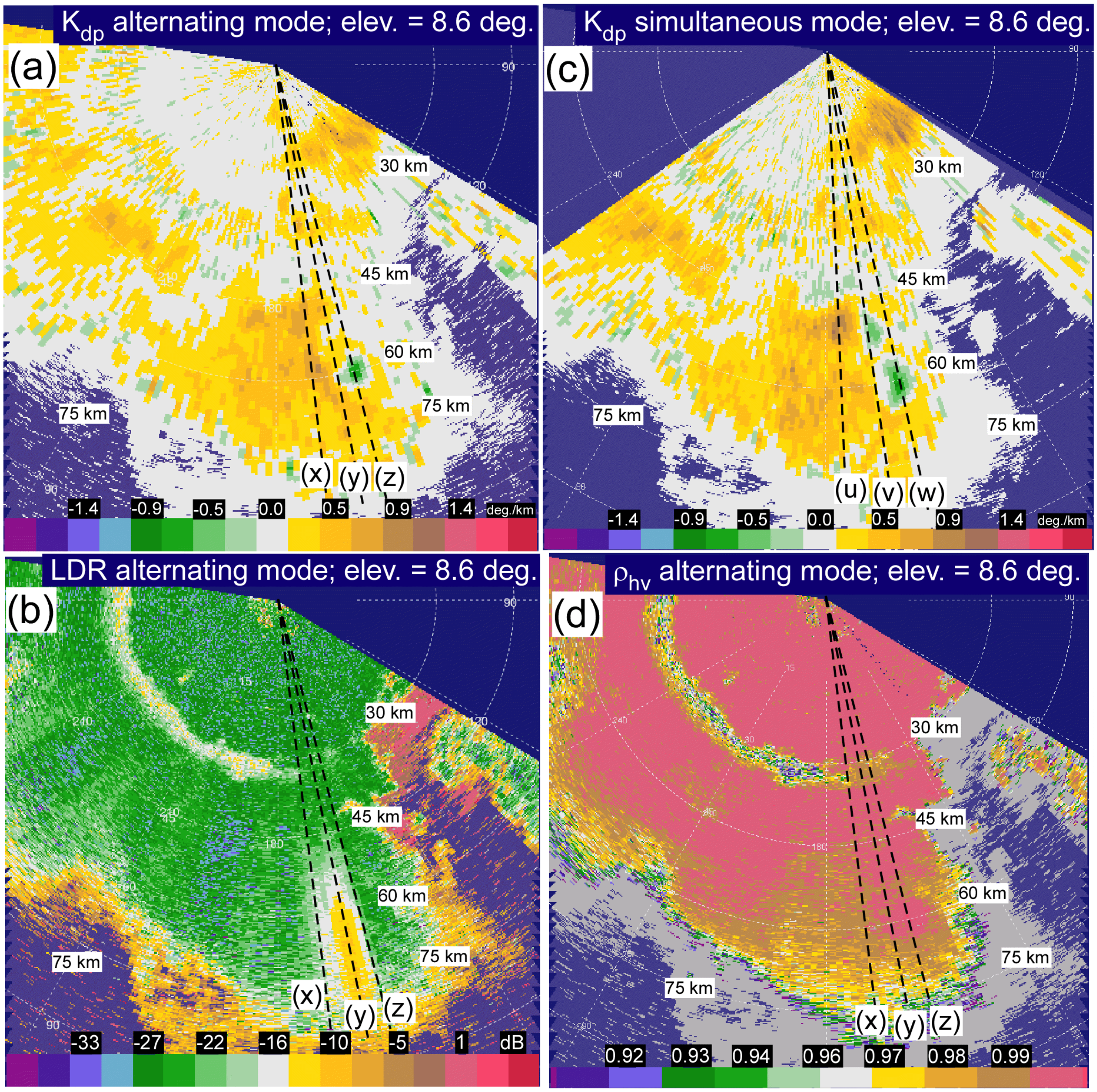

Figure 5: *Data corresponding to Fig. 4: (a)* K_{dp}^{fhv}*, (b)* LDR_h*, (c)* K_{dp}^{shv}*, and (d)* ρ_{hv}*.*

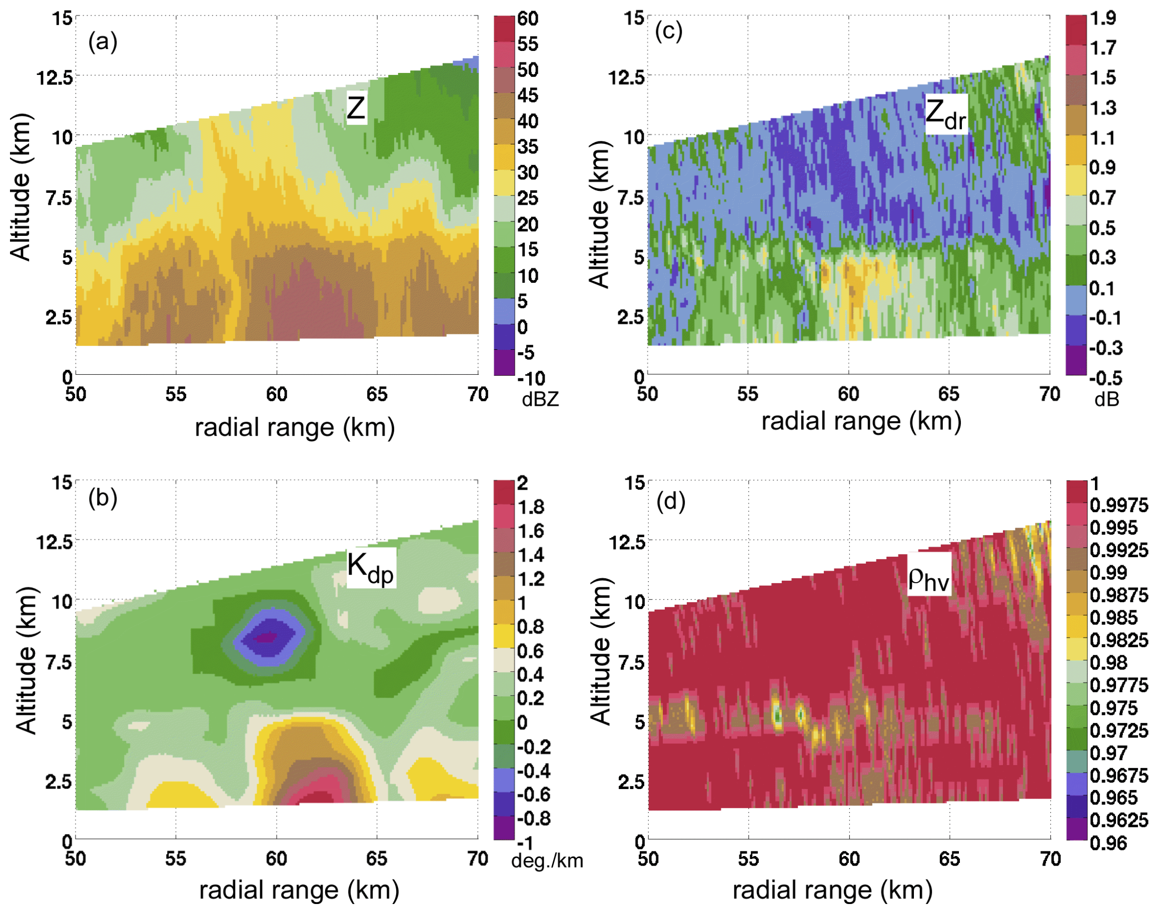

Figure 6: *Vertical FHV data cross sections along line (z) of Fig. 5a that illustrates the negative* K_{dp}^{fhv} *region.*

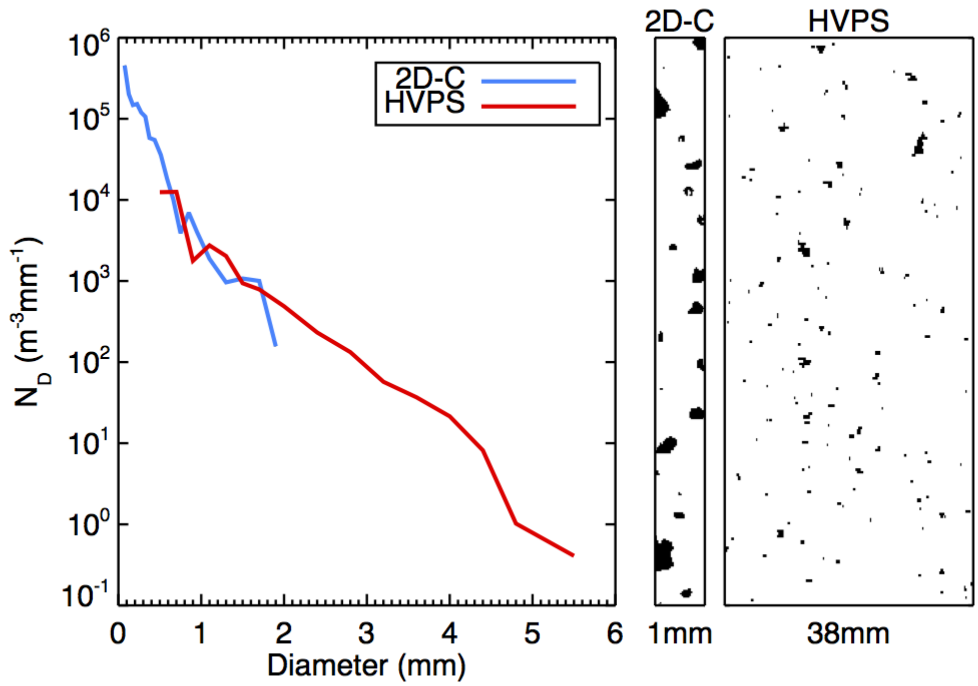

Figure 7: *Particle images and size distributions. Data gathered by the HVPS and 2D-C probes during the ABFM project.*

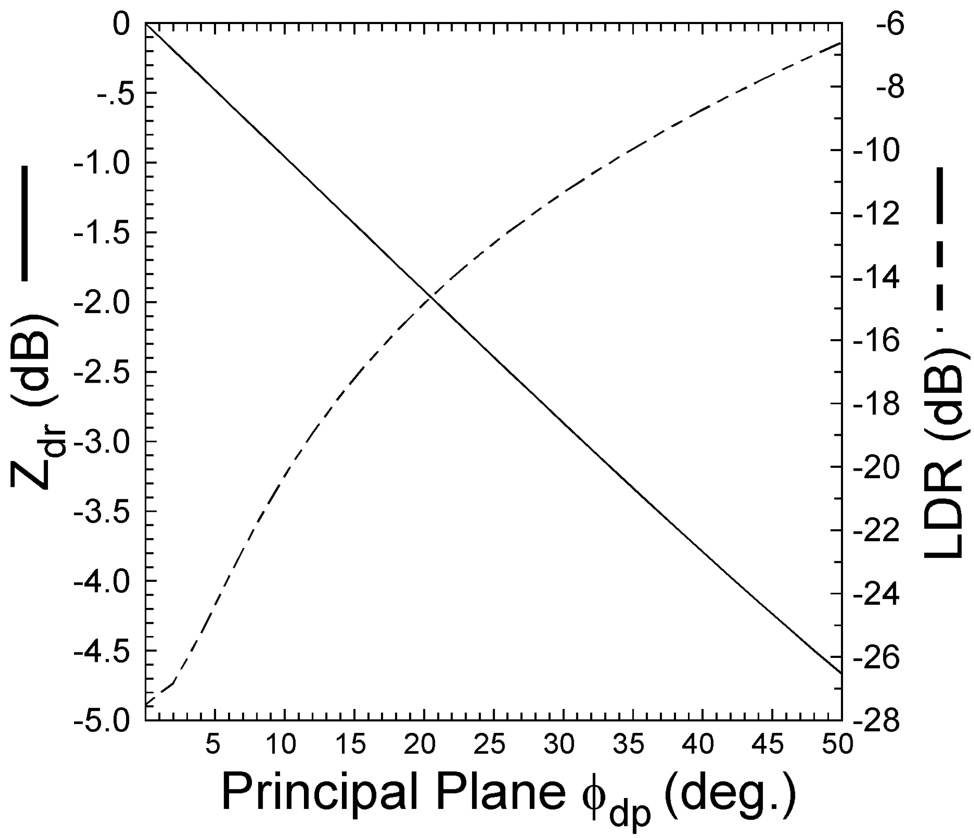

Figure 8: *Modeled bias Z_{dr}^{shv} and LDR_h as a function of Principle Plane ϕ_{dp} (ϕ_{dp}^{pp}). The propagation medium contains ice crystals canted at $45°$ that cause the ϕ_{dp}^{pp} to increase. The backscatter medium contains both the canted ice crystals as well as larger randomly oriented ice particles as described in the text. The intrinsic Z_{dr} and LDR values are seen when $\phi_{dp}^{pp} = 0°$. As ϕ_{dp}^{pp} increases, the bias in Z_{dr}^{shv} and LDR increases rapidly. This explains the Z_{dr}^{shv} and LDR biased striped data seen in Figs. 4e and 5b, respectively.*